Development of an automatic 2D-3D image matching method for reproducing three-dimensional humeral positions using single and dual plane fluoroscopy.

Filipa Pinto Leal
filipa.leal @tecnico.ulisboa.pt

Instituto Superior Técnico, Universidade de Lisboa, Portugal

November 2018

Abstract

The shoulder is a complex system with high clinical relevance. Fluoroscopic image-model techniques have been widely used due to its reported sub-millimeters levels of accuracy. In this study, an automatic 2D-3D image-model matching method was developed to reproduce humerus spatial positions using either dual and single fluoroscopic images. The matching method was accomplished through an optimization process and validated under an idealized environment. By limiting the search space of the optimizer to a range of $[\pm 5\,° ; \pm 5\,mm]$ and $[\pm 20\,° ; \pm 20\,mm]$ from the ideal pose, three objective functions considering simple and complex humerus poses were tested. Using dual fluoroscopic images, the results showed that the minimization of the distances was the objective function which reproduced both type of humerus poses with more accuracy and in agreement with previous studies. The minimization of the areas and moments of inertia showed limited accuracy. Satisfactory results were obtained under the search space of $[\pm 5\,° ; \pm 5\,mm]$, while under the range of $[\pm 20\,° ; \pm 20\,mm]$ less accurate results were obtained. When using single fluoroscopic images, the in-plane accuracy was satisfactory, but at the expense of large out-plane errors. A qualitative analysis of the method under *in vivo* conditions showed poor results. Using the respective fluoroscopic images and 3D models, this method can also be applied to the clavicle and the scapula geometry. In the future, this method can be used to study the shoulder kinematics.

Keywords: Dual plane, Fluoroscopic image, Kinematics, Optimization, Single plane, Shoulder

1. Introduction

The shoulder is the most complex system consisting of three bones (scapula, humerus, clavicle), four joints (glenohumeral, scapulothoracic, acromioclavicular, and sternoclavicular) and a vast number of surrounding tendons and ligaments [1]. The coordinated actions in all articulations give the shoulder mechanism the widest range of motion of all human body [2]. Such large flexibility comes at the cost of intrinsic joint stability being the shoulder joint, the most frequently dislocated joint in the human body [2]. Therefore, it is notorious that the accurate determination of the human shoulder kinematics is a challenging issue in biomedical engineering.

Conventional methods have relied on the use of surface markers. This technique has revealed to be inaccurate for measuring scapula motion due to its flat shape, soft tissue covering and its significant subcutaneous motion [3]. This technique has also revealed to be inadequate for the humerus, since the glenohumeral joint center, important to define its longitudinal axis, is not a palpable bony landmark, and thus has to be estimated [2]. Other techniques have used direct insertion of pins to measure shoulder kinematics, especially the clavicle. As the clavicle only has two bony landmarks, its axial rotation cannot be calculated through non-invasive techniques [4]. Therefore, new techniques able to accurately determine the shoulder kinematics need to be developed.

The main objective of this work is to develop a method capable of measuring the humerus kinematics and that can be applicable to the clavicle and the scapula, so that in the future an analysis of the shoulder kinematics can be performed. An automatic 2D-3D image matching method is developed to accurately determine humerus poses in 6DOF using single and dual fluoroscopic images. An optimization algorithm is used to automatize the matching process between

projections of 3D humerus models and segmented fluoroscopic images. The accuracy of the method is evaluated under an idealized and *in vivo* environment. The sensibility of the algorithm to the size of the search space, different objective functions and humerus poses are tested.

2. Materials and Methods

2.1. 3D Model reconstruction

The subject used in this study is CT imaged to acquires CT images of the humerus. These images are used to construct a 3D anatomical surface mesh of the humerus using the ITK-Snap software. This surface mesh of the humerus is exported to MeshLab, an open source software for processing and editing 3D triangular meshes. In order to smooth staircase artefacts derived from CT scanning, the 3D humerus model undergone a filtering correction. The final geometry of the 3D humerus model is represented in Figure 2.1.

Figure 1 – Final geometry of the 3D humerus model after a filter correction in Meshlab

Then the 3D surface mesh of the humerus was imported to Matlab© software as a 3D point cloud. The original point cloud was downsampled to decrease computation time.

2.1. Fluoroscopy images segmentation

During the exam, the subject was oriented so that all the right shoulder joint was covered. The subject was asked to move his arm through a series of abduction angles imaged by the fluoroscope. These images are stored electronically with an 8-bit grey scale and a resolution of 1024 × 1024 pixels.

The contours of the humerus from the fluoroscopic images were extracted by segmentation. Active contours method was the segmentation technique used. Firstly, a ROI limiting the humerus bone area was manually defined. This region minimizes the presence of the clavicle and scapula that will not be segmented. The contours were saved as a list of 2D spatial points.

The final humerus contour after segmentation of the fluoroscopic image is represented in Figure 3.4. Due to the overlap of the humerus head with the scapula and the clavicle on the fluoroscopic image, a perfect humerus geometry was not obtained - the humerus head did not present a total rounded-shape.

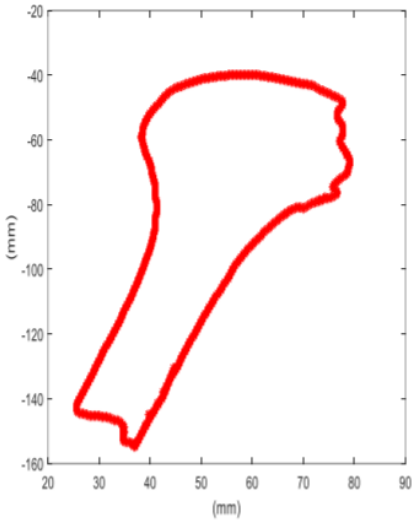

Figure 2 – Humerus contours after segmentation of the single-plane fluoroscopic image

3. Optimized matching method

The matching process was formulated as an optimization procedure that minimizes the error between the projected 3D model and respective fluoroscopic image contours. More precisely, the aim was to determine the optimum 3D bone model pose which makes that the its projection match the outlines captured from the fluoroscopic image taken as the reference. Note that the 3D model pose is defined in 6DOF: the three components of the position vector and the three Euler angles in relation to the global coordinate system. The objective function is a scalar function with six independent variables which define the 3D humerus model.

3.1 Transformation of model points

In the global coordinate system, each point of the 3D model, noted as p_i, is transformed from an

initial pose to a new position and orientation, noted as $\widetilde{p_i}$, by six independent variables. Each point undergoes a 3D translation described by the vector $\mathbf{T} = \{x, y, z\}^T$ and a 3D rotation described by the rotation matrix **R** in (2). The rotation matrix can be defined taking into consideration different rotation sequences. In this case, a Y-Z-X Euler sequence using the angles α, β and γ was applied. The rotation in X corresponds to an α angle, a rotation in Y to a β angle and a rotation in Z to a γ angle.

As soon as the 3D model is transformed to a new pose, the ith point $\widetilde{p_i}$ □, of the 3D model is projected. Depending on the type of fluoroscopic images used, single or dual fluoroscopic images, the 3D humeral model is projected onto one or two planes respectively. Then the boundary points of the resulting 2D model are extracted using the function *boundary* implemented in Matlab©.

$$\widetilde{p_i} = \mathrm{R}\,(p_i) + \mathrm{T} \qquad (1)$$

$$\mathrm{R} = \begin{bmatrix} \cos\beta\cos\gamma & -\sin\gamma & \sin\beta\cos\gamma \\ \cos\alpha\cos\beta\sin\gamma + \sin\alpha\sin\beta & \cos\alpha\cos\gamma & \cos\alpha\sin\beta\sin\gamma - \sin\alpha\cos\beta \\ \sin\alpha\cos\beta\sin\gamma - \cos\alpha\cos\beta & \sin\alpha\cos\gamma & \sin\alpha\sin\beta\,sin\gamma + \cos\alpha\cos\beta \end{bmatrix} \qquad (2)$$

3.2 Objective functions for optimization

To make the projected 3D humerus model match the fluoroscopic outline, different features can be evaluated. Three objective functions were thus tested: the minimization of the moments of inertia, the intersection area and the distance between the projected and fluoroscopic contour points.

3.1.1. Objective Function: Area

The outline points of the projected 3D model and the segmented fluoroscopic image define a 2D polygon. In application of single or dual projection planes k, I_k represents the intersection area between the two polygons and Ref_k the area of the polygon defined by the outlines of segmented fluoroscopic image. The objective function is formulated in (3) and minimizes the difference between I_k and Ref_k. When this difference is equal to zero, the two polygons are completely intersected (Figure 3).

$$J = \sum_{k=1}^{2} (I_k - Ref_k)^2 \qquad (3)$$

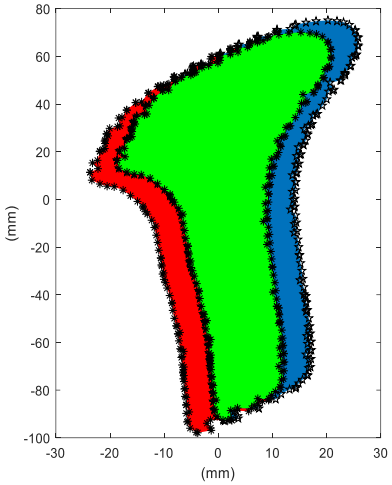

Figure 3 – An iteration of the projected 3D model in red, taken as the reference polygon, and the fluoroscopic model in blue. The green region represents the intersection area of the two models. When the green area equals the blue region the two polygons are totally overlapped.

3.1.2. Objective Function: Distances

For each outline point of the projected 3D model $\widetilde{P_{k,i}}$, the closest point from the fluoroscopic outlines was selected g_k. The distance $d_{k,i}$ between two closest points was calculated using a function already implemented in Matlab®. For each projection plane k, the distances are summed and divided by the total number of points q_k. The resulting normalized distance is returned as the value of the objective function J formulated in (4). The optimization process is thus expressed as the minimization of the distances between the outline points of the projected 3D model and the points of the segmented fluoroscopic image.

$$J = \sum_{k=1}^{2} \frac{1}{q_k} \sum_{i=1}^{q_k} {d_{k,i}}^2 = \sum_{k=1}^{2} \frac{1}{q_k} \sum_{i=1}^{q_k} (g_k - \widetilde{P_{k,i}})^2 \qquad (4)$$

3.1.2. Objective Function: Moments of Inertia

The optimization was defined in this case as the minimization of the difference between the two eigenvalues of the fluoroscopic model ($\lambda_{Ref\,1}$ and $\lambda_{Ref\,2}$) and the projected 3D model ($\lambda 1$ and $\lambda 2$).

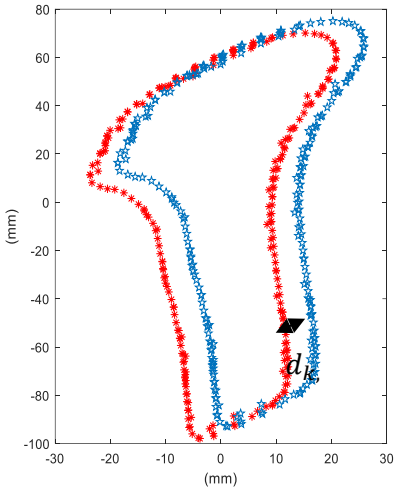

Figure 4. - An iteration of the minimization of the distances between the outline points of the projected 3D model in red and the segmented fluoroscopic image in blue taken as the reference. $d_{k,i}$ represents the distance to be optimized between two closest outline points of the models.

Also, the eigenvectors of the projected 3D model v were ensured to be orthogonal to the eigenvectors of the fluoroscopic model v_{Ref}, i.e their dot product is zero. The objective function J is a combination of these two operations and is formulated by the equation (5) for each projection plane k.

$$J = v_T + \lambda_T$$

$$\lambda_T = \sum_{k=1}^{2} \left(\frac{\lambda_{1,k}}{\lambda_{Ref\ 1,k}} - 1\right)^2 + \left(\frac{\lambda_{2,k}}{\lambda_{Ref\ 2,k}} - 1\right)^2 \quad (5)$$

$$v_T = \sum_{k=1}^{2} (v_{Ref\ 1,k} \cdot v_{2,k})^2 + (v_{Ref\ 2,k} \cdot v_{1,k})^2 \quad (6)$$

The eigenvectors and eigenvalues of the two models were obtained by calculating the tensc (7) inertia I associated to each model.

$$[I] = \begin{bmatrix} Ixx & Ixy \\ Iyx & Iyy \end{bmatrix} \quad (8)$$

$$I_{xx} = \sum_{i=1}^{q_k} m_i y_i^2$$

$$I_{yy} = \sum_{i=1}^{q_k} m_i x_i^2 \quad (9)$$

$$I_{yy} = \sum_{i=1}^{q_k} m_i x_i^2 \quad (10)$$

$$I_{xy} = I_{yx} = -\sum_{i=1}^{q_k} m_i\, x_i y_i \quad (11)$$

Ixx and Iyy are the moments of inertia of the two models with respect to the X and Y axes respectively. The quantities I_{xy}, and $I_{yx}$are the products of inertia. The eigenvectors of I represent the principal axes of the model, the directions about which the object's resistances to rotation is distributed evenly. The eigenvalues are associated to the magnitude of the vectors. Notice that through these operations, only the rotation components of the 3D model are optimized. To optimize the respective translation components, the distance between the centroids of the two models would have to be minimized.

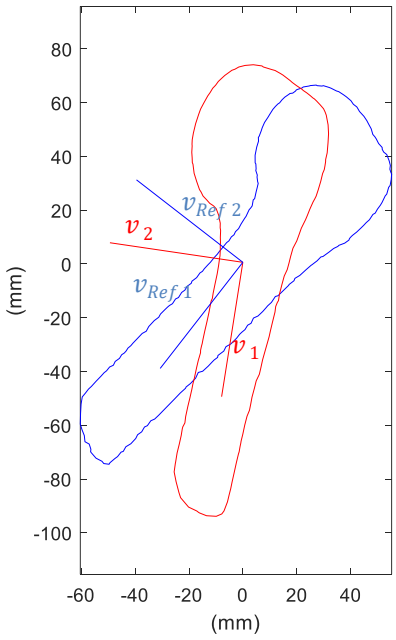

Figure 5 – An iteration of the optimization process between the eigenvectors and eigenvalues of the projected 3D model in red (v) and the model from the fluoroscopic images in blue (v_{Ref}). The models were superimposed. The origin of the orthogonal axes represents the centroid of the two models, The objective is to make that these orthogonal axes coincide.

3.3 Validation

The minimization of the three objective functions was accomplished with a gradient-free based algorithm - the genetic algorithm. This algorithm is implemented on the Matlab© software. The minimization routine is said to converge if the average relative change in the value of the objective function over the iterations is less than or equal to 10^{-4} or when the number of iterations exceeds 200. To validate the accuracy of the method in reproducing the 6DOF spatial positions of the humerus, the algorithm was tested in an idealized and in vivo environment. An idealized testing environment was created to isolate systematic errors and bias related to the geometry of the humerus and extraction of contours from the fluoroscopic images [5]. To assess the performance of the algorithm when running real data, an in vivo test was performed. This test consists on using in vivo fluoroscopic images from one living subject.

3.3.1 Idealized Environment Test

Defining five different poses of the 3D model, five idealized fluoroscopic images were created by projecting the 3D model onto one and two plans. Using these poses as reference, the optimization process aimed to find the positions and orientations which were known a priori. The error of the optimized matching process is measured by comparing the optimized pose with the reference pose. Idealized dual fluoroscopic images were obtained by projecting the 3D model onto the XZ and YZ plan. Idealized single fluoroscopic images were also obtained by projecting the 3D humerus model onto the XZ plan.

Five poses were tested (Table 1): three poses with only one rotation about one axis (SP) and two poses with rotations and translations about the three axes randomly generated using a Gaussian distribution (RGP).

Table 1 – Orientation and position of the five idealized humerus poses

	Rotation			Translation		
	α (°)	β (°)	γ (°)	x (mm)	y (mm)	z (mm)
SP1	0	0	0	0	0	0
SP2	60	0	0	0	0	0
SP3	30	0	0	0	0	0
RGP1	100.04	-38.56	-110.58	7.90	-11.61	12.41
RGP2	-93.51	54.20	-98.49	14.73	8.70	17.32

Under idealized environment the minimization of the areas, distances and moments of inertia were tested. The sensitivity of the algorithm was tested by constraining the search space of the optimizer to a specific range from the ideal poses. A range of ± 5 mm in translation and ± 5 ° in rotation and a range of ± 20 mm in translation and ± 20 ° in rotation from the ideal pose were tested. This optimization procedure was performed 20 times for each humerus pose. The error was measured from the optimized pose to the reference pose.

3.3.2 In Vivo Test

This test employed *in vivo* single fluoroscopic images of the humerus of one living subject. Only one fluoroscopic image of the humerus was selected to test the automatic matching algorithm. The segmented fluoroscopic images are now the reference pose that the projected 3D model needs to match. The selected pose was submitted to a 20 independent optimizations. The objective function used was the minimization of the distances. The accuracy of the automatic 2D-3D matching algorithm in this test was not quantified as no reference was present to know the actual spatial position and orientation of the humerus. Only a qualitative analysis of the results was performed by graphically evaluating if the two matching models were satisfactory overlapped and aligned. In this study, the magnification factor was not able to be calculated. This magnification factor allows to obtain the fluoroscopic humerus contours with the right proportion in relation to its actual size [37]

Given some limitations associated to this test, as segmentation errors and the inexistence of the exact magnification factor, the final positions and orientations of the humerus resulted from the first optimization were submitted to a second optimization process. To achieve better results, the search space and convergence criteria were extended. The search space was constrained to a range of ±30 mm in translation and ±30 ° in rotation from the final positions and orientations obtained from the first optimization. The convergence criteria was extended to a maximum number of generations of 500 and a function tolerance of 10^{-6}.

4. Results

4.1 Idealized environment test

This test evaluated the accuracy of the method in determining known humerus poses using idealized dual and single fluoroscopic images. The three objective functions were tested constraining the search space of the optimizer for a range of $[\pm 5\,mm;\ \pm 5\,^{\circ}]$ and $[\pm 20\,mm;\ \pm 20\,^{\circ}]$ from the ideal pose

4.1.1 Search space: ± 5 mm in translation and ±5° in rotation

For the minimization of the distances, the three SP recorded a maximum error of 0.04 ±0.03° in rotation and errors considered null in translation. In turn, the two RGP were reproduced with a maximum error of 0.64 ± 0.48° in rotation and 0.00 mm in translation (Table 2)

For the minimization of the intersection areas, the errors in rotation and translation were higher than those obtained with the minimization of the distances. The three SP recorded higher errors in γ than in β and α. For these poses, the maximum error in γ reached 2.80 ±1,09° and 0.52 ±0.23 ° for the other two angles. In relation to the translation components, the three SP recorded a maximum error of 0,19 ±0,43 mm. For RGP, this pattern was not so obviously observed - for each RGP, the maximum error in rotation occurred in different variables. Considering the three best optimizations, lower errors in rotation and translation were found (Table 4). The three SP recorded a maximum error in γ of 1.19 ±1.00 ° and 0.11 ±0.03° in the two other angles. The translation components recorded a maximum error of 0.69 ±0.96 mm. For the two RGP, a maximum error of 1.50 ±0.69 ° in rotation and 0.55 ±0.66 mm in translation was recorded (Table 2).

For the minimization of the moments of inertia, the errors obtained were higher than those obtained with the minimization of the distances (Table 2). Likely, these errors were similar to those obtained with the minimization of the areas. The three SP recorded higher errors in γ than in β and α. A maximum error in γ of 0.73 ±1.00 ° and 0.73 ±0.43 ° for the two other angles was recorded. For the two RGP, the maximum error reached 2,02 ±1,43 °. Considering the three best optimizations, a slight decrease on the errors of SP and RGP was observed. A maximum error of 0.56 ° and 1.92 ° was recorded for SP and RGP respectively (Table 4).

4.1 Search space: ± 20 mm in translation and ± 20 ° in rotation

Under this range, for the minimization of the distances, SP were reproduced with the same errors in rotation and translation than those obtained with the range of [± 5 mm; ±5 °]. The RGP were reproduced with an error of 0.00 mm translation and a maximum error of 1.39 ° in rotation, a value slightly higher than that obtained with the range of [± 5 mm; ±5 °] (Table 3).

With the minimization of the intersection areas and the moments of inertia, both RGP and SP recorded higher errors in translation and rotation than those obtained with the previous range. Likely, the SP continued to record higher errors in γ than in α and β. This behavior was not so obviously detected with the RGP, as happened with the previous range.

Considering the three best optimizations for the minimization of the areas, the maximum errors were lower than those obtained with the 20 optimizations, but still high (Table 5). SP were reproduced with a maximum error of 9.18 ±0.08° in rotation and 0.81 ±1.02 mm in translation. RGP were reproduced with a maximum error of 5,64 ±0.85 ° in rotation and 0.73 ±0.31 mm in translation.

When only the three best optimizations were considered for the minimization of the moments of inertia, the errors were still high (Table 5). SP were reproduced with a maximum error of 7.17 ±4.55 ° in γ and 1.73 ±1.38 ° on the two other angles. RGP were reproduced with a maximum error of 3.98 ±2.84°.

4.1.3 Single Plane Optimization

Since the minimization of the distances was the objective function which yielded the most accurate results, single plane optimization was also tested with this function.

For the range of [± 5 *mm*; ±5 °], the three SP recorded a maximum in-plane error of 0,01 ± 0,01° in rotation and 0.00 mm translation. Along the out-plane direction higher errors in translation were recorded, with a maximum of 2.53 ±1.34 *mm* . For the RGP, an in-plane error of 1.18 ° in rotation and 0.00 mm in translation, with a maximum out-plane error of 0.96 ° in rotation and 2.84 *mm* in translation was recorded (Table 6) . For the range of [± 20 *mm*; ± 20 °], the same behavior was observed: low in-plane errors at the expense of large out-of-plane errors. These values were specially elevated for RGP. RGP recorded a maximum in-plane error of 3.14 ° in rotation and 0,70 *mm* in translation, with a maximum out-plane error of 2.73 ±2.71° in rotation and 10.73 ±5.79 *mm* in translation (Table 7).

Table 2 - Mean absolute error associated to each pose when using the three objective functions and idealized dual fluoroscopic outlines and a search range of [± 5 *mm*; ± 5 °] from the ideal pose.

	Model Pose	Rotation (°)			Translation (*mm*)		
		$\Delta\alpha$	$\Delta\beta$	$\Delta\gamma$	Δx	Δy	Δz
Distances	RGP1	0,13 ± 0,13	0,11 ± 0,11	0,05 ± 0,05	0,00 ± 0,00	0,00 ± 0,00	0,00 ± 0,00
	RGP2	0,63 ± 0,48	0,64 ± 0,48	0,07 ± 0,05	0,00 ± 0,00	0,00 ± 0,00	0,00 ± 0,00
	SP1	0,01 ± 0,01	0,02 ± 0,03	0,04 ± 0,03	0,00 ± 0,00	0,00 ± 0,00	0,00 ± 0,00
	SP2	0,01 ± 0,01	0,01 ± 0,01	0,02 ± 0,02	0,00 ± 0,00	0,00 ± 0,00	0,00 ± 0,00
	SP3	0,00 ± 0,00	0,03 ± 0,05	0,02 ± 0,04	0.00 ± 0,01	0,00 ± 0,00	0,00 ± 0,00
Areas	RGP1	2.99 ±1.38	1.62 ±0.73	1.55 ± 0.74	0.31 ± 0.22	0.85 ± 0.77	0.43 ± 0.31
	RGP2	0.88 ± 0.80	0.90 ±0.82	0.09 ± 0.09	0.00 ± 0.00	0.00 ± 0.00	0.00 ± 0.00
	SP1	0.02 ± 0.02	0.19 ±0.24	0.87 ± 1.12	0.07 ± 0.11	0.01 ± 0.01	0.02 ± 0.03
	SP2	0.07 ± 0.04	0.24 ±0.13	1.43 ± 0.79	0.01 ± 0.01	0.00 ± 0.00	0.01 ± 0.01
	SP3	0.15 ± 0.12	0.52 ±0.23	2.80 ± 1.09	0.05 ± 0.08	0.18 ± 0.19	0.19 ± 0.43
Moments of Inertia	RGP1	0.67 ± 0.55	0.89 ± 0.47	0.89 ± 0.62			
	RGP2	2.02 ± 1.43	1.80 ± 1.21	0.41 ± 0.23			
	SP1	0.43 ± 0.37	0.31 ± 0.25	0.73 ± 1.00			
	SP2	0.17 ± 0.17	0.38 ± 0.27	0.65 ± 0.68			
	SP3	0.20 ± 0.21	0.29 ± 0.21	0.42 ± 0.52			

Table 3 - Mean absolute error associated to each pose when using the three objective functions and idealized dual fluoroscopic outlines and a search range of [± 20 *mm*; ± 20 °] from the ideal pose.

	Model Pose	Rotation (°)			Translation (*mm*)		
		$\Delta\alpha$	$\Delta\beta$	$\Delta\gamma$	Δx	Δy	Δz
Distances	RGP1	0,17 ± 0,21	0,15 ± 0,2	0,06 ± 0,08	0,00 ± 0,00	0,00 ± 0,00	0,01 ± 0,01
	RGP2	1,37 ± 1,29	1,39 ± 1,31	0,14 ± 0,11	0,00 ± 0,01	0,00 ± 0,01	0,00 ± 0,00
	SP1	0,01 ± 0,01	0,01 ± 0,01	0,02 ± 0,02	0,00 ± 0,00	0,00 ± 0,00	0,00 ± 0,00
	SP2	0,01 ± 0,01	0,01 ± 0,01	0,01 ± 0,02	0,00 ± 0,00	0,00 ± 0,00	0,00 ± 0,00
	SP3	0,01 ± 0,01	0,06 ± 0,1	0,05 ± 0,08	0,01 ± 0,02	0,00 ± 0,00	0,00 ± 0,00
Areas	RGP1	9.77 ± 2.97	6.43 ±2.97	5.66 ± 2.10	0.57 ± 0.36	0.78 ± 0.62	0.76 ± 0.59
	RGP2	1.12 ± 0.96	1.15 ±0.99	0.12 ± 0.10	0.00 ± 0.00	0.00 ± 0.01	0.00 ± 0.01
	SP1	0.03 ± 0.03	0.57 ±0.46	2.18 ± 1.81	0.12 ± 0.10	0.03 ± 0.03	0.02 ± 0.03
	SP2	0.60 ± 0.06	1.77 ±0.24	10.14 ± 0.92	0.08 ± 0.05	0.07 ± 0.01	0.08 ± 0.01
	SP3	0.46 ± 0.43	2.30 ±1.40	11.17 ± 5.86	0.29 ± 0.24	0.39 ± 0.46	0.36 ± 0.52
Moments of Inertia	RGP1	4,57 ±4,36	4,86 ±5,09	2,86 ±3,77			
	RGP2	6,61 ± 4,38	9,86 ± 4,21	2,26 ± 1,29			
	SP1	1,43 ± 0,88	1,67 ± 1,1	4,23 ± 5,48			
	SP2	1,39 ± 0,98	1,16 ± 0,88	6,82 ± 4,66			
	SP3	0,79 ± 0,55	0,80 ± 0,50	1,41 ± 1,50			

Table 4 - Mean absolute error associated to each pose considering the three best optimizations, the minimization of the areas and moments of inertia, idealized dual fluoroscopic images and a search range of [± 5 *mm*; ±5 °] from the ideal pose.

	Model Pose	Rotation (°)			Translation (*mm*)		
		$\Delta\alpha$	$\Delta\beta$	$\Delta\gamma$	Δx	Δy	Δz
Areas	RGP1	1.5 ± 0.69	0.88 ± 0.28	0.74 ± 0.36	0.11 ± 0.07	0.55 ± 0.66	0.15 ± 0.08
	RGP2	0.14 ± 0.06	0.14 ± 0.06	0.01 ± 0.01	0.00 ± 0.00	0.00 ± 0.00	0.00 ± 0.00
	SP1	0.00 ± 0.00	0.01 ± 0.00	0.02 ± 0.01	0.00 ± 0.00	0.00 ± 0.00	0.00 ± 0.00
	SP2	0.01 ±0.00	0.03 ± 0.02	0.13 ± 0.08	0.00 ± 0.00	0.00 ± 0.00	0.00 ± 0.00
	SP3	0.10 ± 0.03	0.11 ± 0.03	1.19 ± 1.00	0.12 ± 0.16	0.23 ± 0.3	0.69 ± 0.96
Moments of Inertia	RGP1	0.43 ± 0.33	0.55 ± 0.27	0.64 ± 0.38			
	RGP2	1.92 ± 1.86	1.71 ± 1.00	0.28 ± 0.16			
	SP1	0.31 ± 0.19	0.10 ± 0.04	0.49 ± 0.33			
	SP2	0.14 ± 0.08	0.33 ± 0.19	0.28 ± 0.10			
	SP3	0.18 ± 0.20	0.11 ± 0.07	0.56 ± 0.66			

Table 5 - Mean absolute error associated to each pose considering the three best optimizations, the minimization of the areas and moments of inertia, idealized dual fluoroscopic images and a search range of [± 20 *mm*; ±20 °] from the ideal pose.

	Model Pose	Rotation (°)			Translation (*mm*)		
		$\Delta\alpha$	$\Delta\beta$	$\Delta\gamma$	Δx	Δy	Δz
Areas	RGP1	5.64 ± 0.85	3.05 ± 0.59	2.96 ± 0.52	0.40 ± 0.10	0.73 ± 0.31	0.51 ± 0.22
	RGP2	0.12 ± 0.07	0.13 ± 0.07	0.01 ± 0.01	0.00 ± 0.00	0.00 ± 0.00	0.00 ± 0.00
	SP1	0.01 ± 0.00	0.01 ± 0.00	0.03 ± 0.01	0.00 ± 0.00	0.00 ± 0.00	0.00 ± 0.00
	SP2	0.57 ± 0.04	1.43 ± 0.05	9.18 ± 0.08	0.13 ± 0.04	0.06 ± 0.00	0.09 ± 0
	SP3	0.08 ± 0.05	0.49 ± 0.26	3.43 ± 0.43	0.06 ± 0.05	0.29 ± 0.34	0.81 ± 1.02
Moments of Inertia	RGP1	1.31 ± 1.21	1.36 ± 0.45	1.31 ± 0.92			
	RGP2	3.98 ± 2.84	3.59 ± 1.74	0.36 ± 0,15			
	SP1	0.91 ± 0.69	1.73 ± 1.39	3.17 ± 2.25			
	SP2	0.64 ± 0.23	1.16 ± 0.79	7.17 ± 4.56			
	SP3	0.17 ± 0.06	0.24 ± 0.13	0.23 ± 0.25			

Table 6 - Mean absolute error associated to each pose when using the minimization of the distances, single idealized fluoroscopic outlines and a range of $[\pm 5\,mm;\ \pm 5\,°]$ from the ideal poses. Values referent to a total of 20 optimizations. In-plane (x , z ,β) out-of-plane (α ,γ ,y).

Model Pose	Rotation (°)			Translation (mm)		
	$\Delta\alpha$	$\Delta\beta$	$\Delta\gamma$	Δx	Δy	Δz
RGP1	0.15 ± 0.13	0.15 ± 0.14	0.06 ± 0.05	0.00 ± 0.00	2.62 ± 1.53	0.01 ± 0.01
RGP2	0.96 ± 0.86	1.18 ± 0.9	0.1 ± 0.07	0.01 ± 0.00	2.84 ± 1.32	0.00 ± 0.00
SP1	0.02 ± 0.02	0.01 ± 0.01	0.03 ± 0.02	0.00 ± 0.00	2.32 ± 1.11	0.00 ± 0.00
SP2	0.00 ± 0.00	0.01 ± 0.01	0.01 ± 0.01	0.00 ± 0.00	2.53 ± 0.00	0.00 ± 0.00
SP3	0.01 ± 0	0.01 ± 0.01	0.03 ± 0.04	0.00 ± 0.00	2.52 ± 1.34	0.00 ± 0.00

Table 7 - Mean absolute error associated to each pose when using the minimization of the distances, single idealized fluoroscopic outlines and a range of $[\pm 20\,mm;\ \pm 20\,°]$ from the ideal poses. Values referent to a total of 20 optimizations. In-plane (x , z ,β) out-of-plane (α ,γ ,y).

Model Pose	Rotation (°)			Translation (mm)		
	$\Delta\alpha$	$\Delta\beta$	$\Delta\gamma$	Δx	Δy	Δz
RGP1	0.17 ± 0.21	3.14 ± 6.35	0.4 ± 0.96	0.5 ± 1.27	9.76 ± 5.32	0.70 ± 1.81
RGP2	1.37 ± 1.29	2.86 ± 2.88	0.22 ± 0.21	0.01 ± 0.02	10.73 ± 5.79	0.02 ± 0.03
SP1	0.01 ± 0.01	0.01 ± 0.02	0.04 ± 0.03	0.00 ± 0.00	10.32 ± 6.22	0.00 ± 0.00
SP2	0.01 ± 0.01	0.01 ± 0.00	0.01 ± 0.01	0.00 ± 0.00	11.42 ± 6.23	0.00 ± 0.00
SP3	0.01 ± 0.01	0.01 ± 0.03	0.03 ± 0.05	0.00 ± 0.00	12.81 ± 4.28	0.00 ± 0.00

4.2 In vivo environment test

In general, none of the 20 optimizations generated a satisfactory match between the projected 3D model and the fluoroscopic outlines. Figure 4.1 represents the best match after two successive optimizations. In the first optimization, a considerable part of the head and the body of the humerus does not overlap the model obtained from the segmented fluoroscopic images. Moreover, they are not aligned. After a second optimization process, a greater overlap of the projected 3D model over the model formed by the humerus outlines of the fluoroscopic image is observed, however, they are still not aligned.

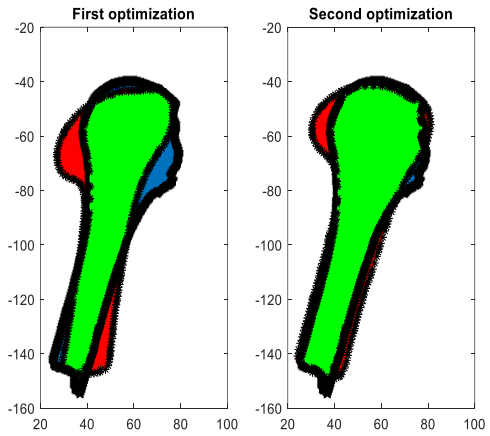

Figure 4: Final match between the projected 3D model (red) and thehumerus outlines from the fluoroscopic images (blue) and respective intersection (green) after a first and second

5. Discussion

In this study, an automatic 2D-3D image matching method was developed to accurately reproduce humerus poses. An optimization algorithm was used to automatize the matching process, the genetic algorithm. The accuracy of the method was evaluated under an idealized environment. Idealized fluoroscopic images were created considering five poses of the 3D humerus model – three poses with only one rotation about one axis (SP) and two poses with rotations and translations about the three axes randomly generated (RGP). Three objective functions were tested when constraining the search space of the optimizer to a range of ± 5 mm in translation and ± 5 ° in rotation and a range of ± 20 mm and ± 20 ° from the ideal pose.

The minimization of the distances was the objective function which showed more accuracy in reproducing both RGP and SP poses in space for both ranges. The errors for RGP were slightly higher than SP but still accurate. The results showed to be very consistent given the reduced standard deviation associated and the similar results obtained for both ranges. With dual fluoroscopic images and the range of [± 5 ° ;± 5 mm], SP recorded optimum error values of 0.02 ° in rotation and error zero values in translation. The RGP recorded errors of 0.63 ° in rotation and error zero values in translation. For the range of [± 20 ° ;± 20 mm], SP recorded a maximum error of 0.05 ° in rotation and error zero values in translation. The RGP recorded a maximum error of 1.37 ° in rotation and zero value errors in translation.

Higher error values were obtained when using the minimization of the moments of inertia and the intersection area with ideal dual fluoroscopic images. This result demonstrates that the algorithm used might have more sensitivity to optimize the distances than the areas and moments of inertia. With these two objective functions, the SP recorded higher errors in γ than in β and α. This result is likely due to the two projections have occurred in the plane XZ and YZ. These two planes are perpendicular to Y and X respectively, which allow a better approximation of the correspondent angles, β and α. For a better approximation of γ, a projection in the perpendicular plane to the axis associated to γ would have to be made, i.e. in the XY plane. This behavior is not specially detected for RGP possibly due to the complexity of the rotations and translations associated. Considering only the three best optimizations, more accurate results were obtained, especially for the range [± 5 ° ;± 5 mm]. For the range of [± 20 ° ;± 20 mm], both RGP and SP were still reproduced with high errors associated. These results suggest that these two objective functions have limited accuracy. Its

performance is dependent on the size of the search space applied to the optimizer. Better results were attained with the range of [±5 °; ± 5 mm] than with a range of [±20 °; ± 20 mm] since when constraining the set of possible solutions to a narrower range, the optimizer is more likely to find an optimum solution.

The use of the minimization of the moments of inertia have limited applicability. Firstly only the rotation components of the model can be optimized. Secondly, in case of the two models have different sizes, which may happen under an in vivo test, the principal axes of the models are also different which becomes difficult the alignment of the two models. Also, the use of the minimization of the areas cannot be generalized to all situations. In case the model from the fluoroscopic image is larger than the projected 3D model or vice-versa, the optimizer only ensures the two models are totally overlapped. The optimizer does not ensure the models are aligned. The minimization of the distances is the objective function which provides more robust results. By calculating the distance between the two models, a correspondence between the points is established, making that this function may be applied even in cases de two models have different sizes.

For idealized single fluoroscopic images, for the range of [± 5 ° ;± 5 mm], SP and RGP were accurately reproduced in the imaging plane (x,z,β), but at the expense of large errors along the out-plane direction. This behavior was also found with the range of [± 20 ° ;± 20 mm] but with higher errors associated. This test highlights the accuracy of dual plane optimization over single plane optimization. This is because out-of-plane errors of one projection are the in-plane errors of the other projection. Thus if in-plane motion is the primary measurement, this method can provide satisfactory accuracy using only single fluoroscopic images. If an analysis of the kinematics with 6DOF is the goal, dual plane optimization is necessary for sub-millimeter-degree resolution in all planes.

In a general way, the results obtained compare positively to previous studies which also used an automatic 2D-3D image model technique for determining bone positions in 6DOF. In a study of shoulder kinematics, Z.Zhu et al. determined humerus positions in space using a gradient-based algorithm to minimize the distances between the two matching models. This type of algorithms needs a humerus initial pose so that the optimization can start. For an idealized environment, the initial pose was randomly generated within the range of ± 5 ° in rotation and ± 5 mm in translation from the ideal pose [5]. Maximum errors of 0,03 mm in translation and 0,07 ° in rotation were found using dual fluoroscopic images [5]. For single fluoroscopic images, accurate results in in-plane motion were recorded at the expense of large out-plane errors. The algorithm used in this study is not dependent on a single initial pose. GA starts with a set of initial poses (400) with the search space constrained to a specific range. Constraining the search space to [± 5 °;± 5 mm] from the ideal pose, the minimization of the distances, and ideal dual fluoroscopic images, the results obtained with the presented method are consistent with those published, using both SP and RGP. For idealized single fluoroscopic images the same behavior of accurate in-plane results at the expense of large out-plane errors is observed for both RGP and SP.
Bingham and Li applied the same methodology as before to determine flexion positions of the tibia and femur using dual fluoroscopic images [6]. This study used a range of ± 20 ° in rotation and ± 20 mm to create the initial poses. Errors of 0,07 mm in translation and 0,16 ° in rotation were recorded to determine femoral and tibial poses. In a study with single fluoroscopic images, Z. Zhu and G. Li found that spatial poses of the femur and tibia can be determined with high accuracy in in-plane at the expense of large out-plane errors. Despite the different bone geometries, when a constraint range of [± 20 °;± 20 mm] was used, the results from this study can be favorably compared to those from [6] and [7] if SP was used as reference. With RGP, the error values obtained with the presented method were higher.

For the *in vivo* test, the data showed that even after a second optimization of the results, the matching models were still not aligned. Two important factors may have contributed to the poor results. Firstly, the segmentation of the fluoroscopic images was susceptible to some errors, causing some geometric changes in the humerus natural morphology. Secondly, it was used an approximation of the magnification factor. This led to the use of fluoroscopic outlines with an inaccurate proportion, making the optimization process had occurred between models with different sizes.

The clavicle and the scapula present some characteristics that make them impossible to be accurately analyzed by the conventional methods. The scapula does not allow an accurate tracking through the use of surface markers because of its flat shape, soft tissue covering and significant subcutaneous motion [3]. Regarding the clavicle, only two bony landmarks are palpable, making that its axial rotation cannot be calculated through non-invasive techniques [4]. The presented method allows the kinematic analysis of any bony structure as long as the respective 3D model and fluoroscopic images are available. This technique can thus be a powerful tool to study the clavicle and the scapula kinematics. Moreover, this technique allows a dynamic motion analysis, conversely to 3D static

analysis usually applied. This optimized image matching method permit the processing of large quantities of image sets describing a dynamic motion. This is not so easily achieved if the matching process is performed in a manual way, as demonstrated in [1], where the 3D model is manually manipulated in space so that its projection match the fluoroscopy image.

The validation of the automatic matching algorithm to reproduce humerus positions in space has certain limitations. For the difficulty of establishing an in vivo gold standard pose of the humerus, only a qualitative analysis concerning the accuracy of the method under in vivo conditions was performed. For the same reason, the accuracy of the method was indirectly evaluated under idealized conditions which did not take into account possible effects of image segmentation.

In conclusion, this methodology could be a useful tool for investigating the kinematics of the human body. However, more in vivo test should be performed to understand the limits of the applicability of the method. With further research could be readily applied to study the shoulder kinematics.

References

[1] M. J. Bey, R. Zauel, S. K. Brock, e S. Tashman, «Validation of a New Model-Based Tracking Technique for Measuring Three-Dimensional, In Vivo Glenohumeral Joint Kinematics», *J. Biomech. Eng.*, vol. 128, n. 4, p. 604, 2006.

[2] C. Quental, J. Folgado, J. Ambrósio, e J. Monteiro, «A multibody biomechanical model of the upper limb including the shoulder girdle», *Multibody Syst. Dyn.*, vol. 28, n. 1, pp. 83–108, Ago. 2012.

[3] P. W. McClure, L. A. Michener, B. J. Sennett, e A. R. Karduna, «Direct 3-dimensional measurement of scapular kinematics during dynamic movements in vivo», *J. Shoulder Elbow Surg.*, vol. 10, n. 3, pp. 269–277, Mai. 2001.

[4] G. Wu *et al.*, «ISB recommendation on definitions of joint coordinate systems of various joints for the reporting of human joint motion—Part II: shoulder, elbow, wrist and hand», *J. Biomech.*, vol. 38, n. 5, pp. 981–992, Mai. 2005.

[5] Z. Zhu, D. F. Massimini, G. Wang, J. J. P. Warner, e G. Li, «The accuracy and repeatability of an automatic 2D–3D fluoroscopic image-model registration technique for determining shoulder joint kinematics», *Med. Eng. Phys.*, vol. 34, n. 9, pp. 1303–1309, Nov. 2012.

[6] J. Bingham e G. Li, «An Optimized Image Matching Method for Determining In-Vivo TKA Kinematics with a Dual-Orthogonal Fluoroscopic Imaging System», *J. Biomech. Eng.*, vol. 128, n. 4, p. 588, 2006.

[7] Z. Zhu e G. Li, «An automatic 2D–3D image matching method for reproducing spatial knee joint positions using single or dual fluoroscopic images», *Comput. Methods Biomech. Biomed. Engin.*, vol. 15, n. 11, pp. 1245–1256, Nov. 2012.